AIAA JOURNAL
Vol. 36, No. 9, September 1998

# Low-Diffusion Flux-Splitting Methods for Flows at All Speeds

Jack R. Edwards*
*North Carolina State University, Raleigh, North Carolina 27695*
and
Meng-Sing Liou†
*NASA Lewis Research Center, Cleveland, Ohio 44135*

**Methods for extending the advective upwind splitting method (AUSM) family of low-diffusion flux-splitting schemes to operate effectively at all flow speeds are developed. The extensions developed are designed for use with time-derivative preconditioning and are based on the idea that the speed of sound should cease to be an important scaling parameter for the diffusive contributions to the interface flux as the Mach number becomes small. Using this criterion, alternative definitions for the interface Mach numbers are developed, and methods for ensuring pressure–velocity coupling at low speeds are formulated. Results are presented for inviscid flows through a channel at various Mach numbers, developing viscous flow in a two-dimensional duct, driven-cavity flows at various Mach and Reynolds numbers, flow over a backward-facing step, and hydrogen–nitrogen mixing layers.**

## I. Introduction

RECENT developments[1–7] have shown the utility of low-diffusion flux-splitting schemes [advective upwind splitting method (AUSM), AUSM+, and variants] in the resolution of gas-dynamic phenomena. Such approaches can be viewed as a rational means of removing excessive numerical diffusion inherent in flux-vector splitting methods while preserving solution monotonicity and numerical stability. The result is a class of methods competitive with flux-difference splitting schemes in terms of accuracy but having a lower per-equation cost. As with most upwind methods, the interface flux formulas for low-diffusion flux-splitting schemes can be written as a central difference contribution plus a diffusive contribution. Differences among the various approaches relate primarily to the behavior of the diffusive contribution at the critical sonic and stagnation points. As such, the discontinuity-capturing traits of the schemes can vary quite widely. A feature common to all approaches, however, is the scaling of components of the diffusive contribution by the speed of sound.

A parallel trend in computational fluid dynamics has resulted in the development of time-derivative preconditioning techniques for integrating the Euler and Navier–Stokes equations.[8–13] Such methods seek to modify the time component of the Euler/Navier–Stokes set so that the condition number remains bounded, independent of the Mach number of the flow. This property is most useful in the computation of very low-speed, compressible flows, serving to bridge the gap between density-based, strongly coupled methods of time integration and sequential, pressure-based iteration algorithms.[12] Recent studies have shown that solution accuracy at low speeds can be compromised if the numerical flux formulation is not modified to reflect the eigensystem of the preconditioned equations.[9,10]

The present contribution is designed to extend the AUSM family of low-diffusion flux-splitting methods to operate effectively in conjunction with time-derivative preconditioning. Anticipated benefits from this extension include enhanced resolution of flow phenomena at all speeds without uncertainties associated with the scaling of added numerical diffusion or the additional complexity associated with Riemann-based approaches.[11] At least one prior attempt at modifying AUSM to operate at all flow speeds has been documented,[14] and similar modifications to the related CUSP (convective upwind split pressure) scheme[15] have been proposed.[16] The major difference between this work and that of Ref. 14 is that in the present study the eigenvalues of the preconditioned system are directly used to effect the transition from a formulation suitable for high-speed flows to one suitable for low-speed flows. Furthermore, the present work provides a general framework for extending related approaches, such as AUSMDV[3] and LDFSS,[6] to operate at all flow speeds. The remainder of this paper proceeds as follows. In Sec. II, the preconditioning strategy of Choi and Merkle[8] (see also Ref. 11) is reviewed, as are other methods for discretizing the preconditioned Euler system. Basic formulations for the AUSM+ and AUSMDV low-diffusion upwind schemes are presented in Sec. III. Section IV discusses modifications necessary to ensure proper behavior at all speeds. The results of this investigation are presented in Sec. V, and some concluding remarks are provided in Sec. VI.

## II. Time-Derivative Preconditioning

The two-dimensional, preconditioned Euler system can be written in Cartesian coordinates as follows:

$$\Gamma\frac{\partial \boldsymbol{W}}{\partial t}+\frac{\partial \boldsymbol{F}}{\partial x}+\frac{\partial \boldsymbol{G}}{\partial y}=0 \tag{1}$$

where $\boldsymbol{W}$ is a vector of primitive variables $[p, u, v, T]^T$. In the present study, the preconditioning matrix $\Gamma$ is based on that proposed by Choi and Merkle[8] and extended further by Weiss and Smith.[11] Given that

$$U_{\text{ref}}^2=\min\left[a^2, \max\left(|\boldsymbol{V}|^2, K|\boldsymbol{V}_\infty|^2\right)\right] \tag{2}$$

$$\Theta=\frac{1}{U_{\text{ref}}^2}-\frac{1}{a^2} \tag{3}$$

$$H=C_pT+\tfrac{1}{2}(u^2+v^2) \tag{4}$$

where $|\boldsymbol{V}|$ is the local velocity magnitude, $|\boldsymbol{V}_\infty|$ is a fixed reference velocity, $a$ is the sound speed, and $K$ is a constant; the preconditioning matrix $\Gamma$ takes the following form:

$$\begin{bmatrix} \Theta+(1/RT) & 0 & 0 & -\rho/T \\ u[\Theta+(1/RT)] & \rho & 0 & -\rho u/T \\ v[\Theta+(1/RT)] & 0 & \rho & -\rho v/T \\ H[\Theta+(1/RT)]-1 & \rho u & \rho v & \rho[C_p-(H/T)] \end{bmatrix} \tag{5}$$

Received May 15, 1997; presented as Paper 97-1862 at the AIAA 13th Computational Fluid Dynamics Conference, Snowmass Village, CO, June 29–July 2, 1997; revision received March 9, 1998; accepted for publication May 4, 1998. 

*Assistant Professor, Department of Mechanical and Aerospace Engineering, Campus Box 7910. E-mail: edwards@jupiter1.mae.ncsu.edu. Senior Member AIAA.

†Senior Scientist, Turbomachinery and Propulsion Systems Division. E-mail: fsmsl@yinyan.lerc.nasa.gov. Associate Fellow AIAA.

As indicated, the Weiss–Smith preconditioner is formed by the addition of the vector $\boldsymbol{\Theta}[1, u, v, T]^T$ to the first column of the Jacobian matrix $\partial \boldsymbol{U}/\partial \boldsymbol{W}$, where $\boldsymbol{U}$ is the vector of conservative variables. Following Turkel et al.,[10] the reference velocity $\boldsymbol{U}_{\text{ref}}$ in Eq. (2) is limited from below by a multiple of $|\boldsymbol{V}_\infty|$ to prevent anomalous behavior at near-stagnation conditions and from above by the sound speed to remove preconditioning for locally supersonic flows. In the present study, $|\boldsymbol{V}_\infty|$ is set to be the average incoming freestream velocity, and $K$ is fixed at 0.25. The eigenvalues of $\Gamma^{-1}A$ ($A = \partial F/\partial \boldsymbol{W}$) are $u$, $u' \pm a'$, where $u$ is the velocity component in the $x$ direction and

$$u' \pm a' = \tfrac{1}{2}\left[\left(1 + M_{\text{ref}}^2\right)u \pm a\sqrt{\left(1 - M_{\text{ref}}^2\right)^2 M^2 + 4M_{\text{ref}}^2}\right] \tag{6}$$

$$M_{\text{ref}}^2 = \frac{U_{\text{ref}}^2}{a^2} \tag{7}$$

$$M = u/a \tag{8}$$

In general, one can express the spatial derivative $\partial F/\partial x$ as a flux balance over a particular mesh cell, with the interface flux $F_{i+1/2}$ defined as consisting of a central difference contribution plus a diffusive contribution $\mathcal{D}$:

$$\boldsymbol{F}_{i+\frac{1}{2}} = \tfrac{1}{2}[\boldsymbol{F}_i + \boldsymbol{F}_{i+1} + \mathcal{D}(i, i+1)] \tag{9}$$

To maximize efficiency and accuracy, it is necessary that the artificial diffusion mechanism $\mathcal{D}$ be constructed to reflect the new eigensystem. This can be accomplished on several different levels. In a simple central difference implementation, an appropriate but overly diffusive choice is[13]

$$\mathcal{D}(i, i+1) = (|u'| + a')_{i+\frac{1}{2}}\Gamma_{i+\frac{1}{2}}(\boldsymbol{W}_i - \boldsymbol{W}_{i+1}) \tag{10}$$

which can be approximated as

$$\mathcal{D}(i, i+1) = (|u'| + a')_{i+\frac{1}{2}}\left(\begin{bmatrix} \rho_i - \rho_{i+1} \\ \rho_i u_i - \rho_{i+1}u_{i+1} \\ \rho_i v_i - \rho_{i+1}v_{i+1} \\ \rho_i H_i - \rho_{i+1}H_{i+1} \end{bmatrix} + \begin{bmatrix} 1 \\ u \\ v \\ H \end{bmatrix}_{i+\frac{1}{2}} \boldsymbol{\Theta}_{i+\frac{1}{2}}(p_i - p_{i+1})\right) \tag{11}$$

Another choice is a Roe-type flux-difference splitting[9,11]:

$$\mathcal{D}(i, i+1) = \Gamma_{i+\frac{1}{2}}(T|\Lambda|T^{-1})_{i+\frac{1}{2}}(\boldsymbol{W}_i - \boldsymbol{W}_{i+1}) \tag{12}$$

where $\Lambda$ is the diagonal matrix of eigenvalues and the modal matrices $T$ and $T^{-1}$ are formed from the eigenvectors of $\Gamma^{-1}A$.

## III. AUSM+ and AUSMDV Flux-Splitting Formulations

The present study focuses on two of the newer low-diffusion flux-splitting methods, AUSM+[4,5,7] and AUSMDV.[3,7] The relationship between the two schemes has been discussed more thoroughly in Ref. 7, and only the highlights of the implementation are presented herein. For both methods, the inviscid interface flux $\boldsymbol{F}_{i+1/2}$ in the $x$ direction is split into a convective contribution $\boldsymbol{F}_{1/2}^c$ plus a pressure contribution $\boldsymbol{F}_{1/2}^p$. The two contributions are treated separately. The convective flux is defined as

$$\boldsymbol{F}_{\frac{1}{2}}^c = (\rho u)_{\frac{1}{2}}\begin{bmatrix} 1 \\ u \\ v \\ H \end{bmatrix}_{i/i+1} \tag{13}$$

where state $i$ is chosen for the column vector $(1, u, v, H)^T$ if the interface mass flux $(\rho u)_{1/2}$ is nonnegative and state $i+1$ is chosen if $(\rho u)_{1/2}$ is negative. The pressure flux is defined as

$$\boldsymbol{F}_{\frac{1}{2}}^p = \begin{bmatrix} 0 \\ p_{\frac{1}{2}} \\ 0 \\ 0 \end{bmatrix} \tag{14}$$

The interface quantities $(\rho u)_{1/2}$ and $p_{1/2}$ are expressed in terms of sets of polynomials in Mach number, defined as

$$M_i = u_i \big/ a_{\frac{1}{2}} \tag{15}$$

where $a_{1/2}$ is an interface speed of sound.[5,7] Three sets of polynomials are required:

$$\mathcal{M}_{(1)}^{\pm} = \tfrac{1}{2}(M \pm |M|) \tag{16}$$

$$\mathcal{M}_{(4)}^{\pm} = \begin{cases} \pm\frac{1}{4}(M \pm 1)^2 \pm \frac{1}{8}(M^2 - 1)^2, & |M| < 1 \\ \mathcal{M}_{(1)}^{\pm}, & \text{otherwise} \end{cases} \tag{17}$$

and

$$\mathcal{P}_{(5)}^{\pm} = \begin{cases} \frac{1}{4}(M \pm 1)^2(2 \mp M) \pm \frac{3}{16}M(M^2 - 1)^2, & |M| < 1 \\ (1/M)\mathcal{M}_{(1)}^{\pm}, & \text{otherwise} \end{cases} \tag{18}$$

The numerals in the subscripts of $\mathcal{M}$ and $\mathcal{P}$ indicate the degree of the polynomials. With these, the interface quantities are defined as

$$(\rho u)_{\frac{1}{2}} = a_{\frac{1}{2}}\left(\rho_i m_{\frac{1}{2}}^+ + \rho_{i+1}m_{\frac{1}{2}}^-\right) \tag{19}$$

$$p_{\frac{1}{2}} = \mathcal{P}_{(5)}^+(M_i)p_i + \mathcal{P}_{(5)}^-(M_{i+1})p_{i+1} \tag{20}$$

Differences between AUSM+ and AUSMDV are due to the chosen definitions of $m_{1/2}^{\pm}$. For AUSM+,

$$m_{\frac{1}{2}} = \mathcal{M}_{(4)}^+(M_i) + \mathcal{M}_{(4)}^-(M_{i+1}) \tag{21}$$

$$m_{\frac{1}{2}}^+ = \tfrac{1}{2}\left(m_{\frac{1}{2}} \pm \left|m_{\frac{1}{2}}\right|\right) \tag{22}$$

For AUSMDV,

$$m_{\frac{1}{2}}^+ = \mathcal{M}_{(1)}^+(M_i) + \omega^+\left[\mathcal{M}_{(4)}^+(M_i) - \mathcal{M}_{(1)}^+(M_i)\right] \tag{23}$$

$$m_{\frac{1}{2}}^- = \mathcal{M}_{(1)}^-(M_{i+1}) + \omega^-\left[\mathcal{M}_{(4)}^-(M_{i+1}) - \mathcal{M}_{(1)}^-(M_{i+1})\right] \tag{24}$$

where

$$\omega^+ = \left(\frac{p_i}{\rho_i}\right)\Big/\left[\frac{1}{2}\left(\frac{p_i}{\rho_i} + \frac{p_{i+1}}{\rho_{i+1}}\right)\right] \tag{25}$$

$$\omega^- = \left(\frac{p_{i+1}}{\rho_{i+1}}\right)\Big/\left[\frac{1}{2}\left(\frac{p_i}{\rho_i} + \frac{p_{i+1}}{\rho_{i+1}}\right)\right] \tag{26}$$

As shown later, the inclusion of $\omega^{\pm}$ in the AUSMDV Mach number splittings results in the addition of a pressure-diffusion term to the interface mass flux. The presence of this term ensures monotonicity in the capturing of non-grid-aligned shock waves but can, under certain conditions, give rise to the carbuncle instability for bluff-body flows. The mass flux representation for AUSM+ does not contain a pressure-diffusion term and is not susceptible to the instability.[7]

## IV. Preconditioned AUSM+ and AUSMDV

### Scaling Issues

AUSM+ and AUSMDV can be modified to operate effectively at very low Mach numbers by paying careful attention to the structure of the diffusive contribution to the interface flux. There are two main issues that must be addressed, the first of which is the scaling

of the diffusive contributions by the speed of sound. As an example, consider the simplest subsonic pressure splitting[1]

$$\mathcal{P}^{+}_{(1)}(M_i) = \tfrac{1}{2}(1 + M_i) \tag{27}$$

$$\mathcal{P}^{-}_{(1)}(M_{i+1}) = \tfrac{1}{2}(1 - M_{i+1}) \tag{28}$$

Substituting these expressions into Eq. (20) and expanding into a central-plus-diffusive contribution yields

$$p_{\frac{1}{2}} = \tfrac{1}{2}\Big[p_i + p_{i+1} + \Big(1\Big/2a_{\frac{1}{2}}\Big)(u_i + u_{i+1})(p_i - p_{i+1}) + \Big(1\Big/2a_{\frac{1}{2}}\Big)(p_i + p_{i+1})(u_i - u_{i+1})\Big] \tag{29}$$

The combination $(p_i + p_{i+1})/(2a_{1/2})$ can be approximated as $(1/\gamma)\rho_{1/2}a_{1/2}$, indicating that the first component of the diffusive contribution scales inversely with the speed of sound, whereas the second scales directly with it. The latter scaling, in particular, is inappropriate for very low-speed flows, as the speed of sound is much larger than the velocity components. The result (if obtainable) is an extremely diffusive solution for the velocity field. Similar trends hold for the higher-degree pressure splitting $\mathcal{P}^{\pm}_{(5)}$.

This problem can be remedied by introducing a preconditioned Mach number, related to $u'/a'$ as defined in Eq. (6) and expressed as

$$\tilde{M}_{i,i+1} = \frac{1}{f_{\frac{1}{2}}}M_{i,i+1} = \frac{u_{i,i+1}}{\tilde{a}_{\frac{1}{2}}} \tag{30}$$

where the preconditioned sound speed is given by

$$\tilde{a}_{\frac{1}{2}} \equiv f_{\frac{1}{2}}a_{\frac{1}{2}} \tag{31}$$

The quantity $f_{1/2}$ is determined from the eigenvalues of the preconditioned system

$$f_{\frac{1}{2}} = \frac{\sqrt{\left(1 - M^2_{\mathrm{ref}_{\frac{1}{2}}}\right)^2 M^2_{\frac{1}{2}} + 4M^2_{\mathrm{ref}_{\frac{1}{2}}}}}{\left(1 + M^2_{\mathrm{ref}_{\frac{1}{2}}}\right)} \tag{32}$$

Note that $M$ is a directional quantity, depending on $u$, whereas $M_{\mathrm{ref}}$ as defined in Eq. (7) is coordinate invariant, depending on both $u$ and $v$. The $\frac{1}{2}$ notation indicates the evaluation of $M_{\mathrm{ref}}$ and $M$ using simple arithmetic averages of properties at states $i$ and $i + 1$. New expressions for the interface Mach numbers $\bar{M}_{i,i+1}$ are then defined as follows:

$$\bar{M}_i = \frac{1}{2}\left[\left(1 + M^2_{\mathrm{ref}_{\frac{1}{2}}}\right)\tilde{M}_i + \left(1 - M^2_{\mathrm{ref}_{\frac{1}{2}}}\right)\tilde{M}_{i+1}\right] \tag{33}$$

$$\bar{M}_{i+1} = \frac{1}{2}\left[\left(1 + M^2_{\mathrm{ref}_{\frac{1}{2}}}\right)\tilde{M}_{i+1} + \left(1 - M^2_{\mathrm{ref}_{\frac{1}{2}}}\right)\tilde{M}_i\right] \tag{34}$$

Substituting these values into the subsonic pressure splittings Eqs. (27) and (28) and collecting terms gives

$$p_{\frac{1}{2}} = \frac{1}{2}\left[p_i + p_{i+1} + \frac{1}{2\tilde{a}_{\frac{1}{2}}}(u_i + u_{i+1})(p_i - p_{i+1}) + \frac{M^2_{\mathrm{ref}_{\frac{1}{2}}}}{2\tilde{a}_{\frac{1}{2}}}(p_i + p_{i+1})(u_i - u_{i+1})\right] \tag{35}$$

As the local Mach number approaches zero, the quantity $\tilde{a}_{1/2}$ becomes of the order of the velocity magnitude. The result is that the second component of the diffusive contribution scales with the velocity magnitude, rather than with the speed of sound. The first component increases in importance, scaling inversely with the velocity magnitude. Similar effects are obtained for higher-degree pressure splittings, such as $\mathcal{P}^{\pm}_{(5)}$.

In the most straightforward implementation of the preconditioned AUSM+/AUSMDV flux splittings, the new definitions of the left- and right-state Mach numbers [Eqs. (33) and (34)] and the new definition of the interface sound speed $\tilde{a}_{1/2}$ [Eq. (31)] simply replace the conventional definitions in both the convective and pressure components of the interface flux. The original AUSM+/AUSMDV formulations are approached smoothly as the local Mach number approaches unity. Note that the use of these definitions is not strictly necessary for the convective portions of the AUSM+ and AUSMDV interface fluxes, provided that pressure–velocity coupling is maintained as discussed next. In the interests of uniformity in presentation, the remaining developments assume that the definitions in Eqs. (31–34) are employed throughout.

**Pressure–Velocity Coupling**

The second issue that must be addressed relates to the need for pressure–velocity coupling at low speeds. The developments just outlined force AUSM+/AUSMDV to behave more as a central difference discretization as the Mach number is lowered, raising the possibility of odd–even decoupling for flows with significant pressure variation. A means of alleviating this problem can be found by first considering the interface mass-flux representation for AUSMDV, evaluated using Eqs. (31–34):

$$(\rho u)_{\frac{1}{2}} = \rho_i\tilde{a}_{\frac{1}{2}}\left\{\mathcal{M}^{+}_{(1)}(\bar{M}_i) + \omega^{+}\left[\mathcal{M}^{+}_{(4)}(\bar{M}_i) - \mathcal{M}^{+}_{(1)}(\bar{M}_i)\right]\right\} + \rho_{i+1}\tilde{a}_{\frac{1}{2}}\left\{\mathcal{M}^{-}_{(1)}(\bar{M}_{i+1}) + \omega^{-}\left[\mathcal{M}^{-}_{(4)}(\bar{M}_{i+1}) - \mathcal{M}^{-}_{(1)}(\bar{M}_{i+1})\right]\right\} \tag{36}$$

This may be expanded as follows:

$$(\rho u)_{\frac{1}{2}} = \tilde{a}_{\frac{1}{2}}\left\{\rho_i\mathcal{M}^{+}_{(1)} + \rho_{i+1}\mathcal{M}^{-}_{(1)} + \left(\mathcal{M}^{+}_{(4)} - \mathcal{M}^{+}_{(1)} + \mathcal{M}^{-}_{(4)} - \mathcal{M}^{-}_{(1)}\right) \times \left[(p_i + p_{i+1})\Big/\left(\frac{p_i}{\rho_i} + \frac{p_{i+1}}{\rho_{i+1}}\right)\right] + \left(\mathcal{M}^{+}_{(4)} - \mathcal{M}^{+}_{(1)} - \mathcal{M}^{-}_{(4)} + \mathcal{M}^{-}_{(1)}\right)\left[(p_i - p_{i+1})\Big/\left(\frac{p_i}{\rho_i} + \frac{p_{i+1}}{\rho_{i+1}}\right)\right]\right\} \tag{37}$$

where the dependence of $\mathcal{M}^{+}_{(1),(4)}$ on $\bar{M}_i$ and $\mathcal{M}^{-}_{(1),(4)}$ on $\bar{M}_{i+1}$ is assumed. The first component in Eq. (37) is a simple advective upwind representation for the mass flux, whereas the second and third components are diffusive contributions. The second component provides a stabilizing influence near sonic points, whereas the third provides a measure of pressure diffusion for subsonic Mach numbers. As the interface Mach numbers $\bar{M}_i$ and $\bar{M}_{i+1}$ approach zero, the first and second components of Eq. (37) vanish, and the mass flux approximates the following:

$$(\rho u)_{\frac{1}{2}} \approx (3\gamma/8)\left(\tilde{a}_{\frac{1}{2}}\Big/a^2_{\frac{1}{2}}\right)(p_i - p_{i+1}) \tag{38}$$

which can be represented as

$$(\rho u)_{\frac{1}{2}} \approx (3\gamma/8)\left(f_{\frac{1}{2}}\Big/a_{\frac{1}{2}}\right)(p_i - p_{i+1}) \tag{39}$$

As the reference Mach number $M_{\mathrm{ref}}$ approaches unity, $f_{1/2}$ approaches unity, and the pressure-diffusion component of the interface mass flux scales inversely with the speed of sound. As $M_{\mathrm{ref}}$ becomes small, $\tilde{a}_{1/2}$ scales as the velocity magnitude, meaning that the pressure contribution scales inversely with the speed of sound and directly with the reference Mach number. For low-speed flows, this term will essentially provide no effect. Keeping in mind the premise that the speed of sound should not scale the diffusive contributions for low-speed flows, it becomes necessary to multiply the third component in Eq. (37) by $1/M^2_{\mathrm{ref}_{1/2}}$. This forces the pressure-diffusion component to scale inversely with the velocity magnitude at low speeds, consistent with the modification to the pressure splitting discussed earlier. The effect of this modification can be further illustrated by considering the limiting form of Eq. (37) as obtained for a truly incompressible fluid ($\rho = \mathrm{const}$, $a = \infty$):

$$(\rho u)_{\frac{1}{2}} = \rho u_{\frac{1}{2}} + C\left(u_{\frac{1}{2}}, \boldsymbol{U}_{\mathrm{ref}}\right)\frac{\sqrt{u^2_{\frac{1}{2}} + 4\boldsymbol{U}^2_{\mathrm{ref}}}}{\boldsymbol{U}^2_{\mathrm{ref}}}(p_i - p_{i+1}) \tag{40}$$

where $u_{1/2} = \frac{1}{2}(u_i + u_{i+1})$ and $C$ varies between 0.35 and 0.525, depending on the ratio of $u_{1/2}$ to $\boldsymbol{U}_{\mathrm{ref}}$. Except for minor variations

in $C$, this limiting form is also shared by both the simple artificial diffusion implementation [Eq. (11)] and the preconditioned Roe scheme[11] [Eq. (12)], although the latter also retains an advective upwind contribution. The approach proposed in Ref. 14 also has a similar structure in the incompressible limit. As noted in Ref. 14, this form of the interface mass flux shares a close relationship with the momentum interpolation procedures developed by Rhie and Chow[17] for incompressible flow simulations on collocated (nonstaggered) grids. As illustrated later, the pressure-dependent terms provide a global elliptic smoothing effect, suppressing any tendency toward checkerboard-type odd–even decoupling.

A rearrangement of the modified Eq. (37) results in the following redefinitions for the AUSMDV split Mach numbers $m^{\pm}_{1/2}$:

$$m^{+}_{\frac{1}{2}} = \mathcal{M}^{+}_{(1)}(\bar{M}_i) + \frac{\omega^{+}}{2}\left\{\left(1 + \frac{1}{M^2_{\mathrm{ref}\,\frac{1}{2}}}\right)\left[\mathcal{M}^{+}_{(4)}(\bar{M}_i) - \mathcal{M}^{+}_{(1)}(\bar{M}_i)\right] + \left(1 - \frac{1}{M^2_{\mathrm{ref}\,\frac{1}{2}}}\right)\left[\mathcal{M}^{-}_{(4)}(\bar{M}_{i+1}) - \mathcal{M}^{-}_{(1)}(\bar{M}_{i+1})\right]\right\} \tag{41}$$

$$m^{-}_{\frac{1}{2}} = \mathcal{M}^{-}_{(1)}(\bar{M}_{i+1}) + \frac{\omega^{-}}{2}\left\{\left(1 + \frac{1}{M^2_{\mathrm{ref}\,\frac{1}{2}}}\right) \times \left[\mathcal{M}^{-}_{(4)}(\bar{M}_{i+1}) - \mathcal{M}^{-}_{(1)}(\bar{M}_{i+1})\right] + \left(1 - \frac{1}{M^2_{\mathrm{ref}\,\frac{1}{2}}}\right) \times \left[\mathcal{M}^{+}_{(4)}(\bar{M}_i) - \mathcal{M}^{+}_{(1)}(\bar{M}_i)\right]\right\} \tag{42}$$

These expressions preserve the original form of the second term in Eq. (37), which scales properly with decreasing Mach number.

AUSM+ does not contain a pressure contribution to the interface mass flux. As such, the extension of the preceding argument to AUSM+ necessitates the addition of a term that behaves similarly to the pressure-diffusion component of the modified Eq. (37) for low-speed flows but turns off as the sonic speed is reached. One choice, consistent with the modification to AUSMDV, is given by the following:

$$(\rho u)_{\frac{1}{2}} = (\rho u)_{\frac{1}{2}\,\mathrm{AUSM+}} + \tilde{a}_{\frac{1}{2}}\left(\frac{1}{M^2_{\mathrm{ref}\,\frac{1}{2}}} - 1\right) \times \left[\mathcal{M}^{+}_{(4)}(\bar{M}_i) - \mathcal{M}^{+}_{(1)}(\bar{M}_i) - \mathcal{M}^{-}_{(4)}(\bar{M}_{i+1}) + \mathcal{M}^{-}_{(1)}(\bar{M}_{i+1})\right] \times \left[(p_i - p_{i+1}) \Big/ \left(\frac{p_i}{\rho_i} + \frac{p_{i+1}}{\rho_{i+1}}\right)\right] \tag{43}$$

The second term in Eq. (37) is not added to the AUSM+ interface flux, as proper behavior at sonic transitions is ensured by the definition of $m_{1/2}$ in Eq. (21).

**Summary of Formulations**

In summary, AUSM+/AUSMDV flux-splitting formulations are extended to operate at all speeds by performing the following operations:

1) Replace the interface speed of sound $a_{1/2}$ by the preconditioned speed of sound $\tilde{a}_{1/2} = f_{1/2}a_{1/2}$ [Eq. (31)].

2) Replace the left- and right-state Mach number definitions by those in Eqs. (33) and (34).

3) For AUSMDV, replace the split Mach number definitions $m^{\pm}_{1/2}$ in Eqs. (23) and (24) by those in Eqs. (41) and (42). This version is henceforth denoted AUSMDV(P).

4) For AUSM+, add the corresponding terms in Eq. (43) to the interface mass flux. This version is denoted as AUSM+(P).

5) Complete the flux evaluation by forming $(\rho u)_{1/2}$ and $p_{1/2}$ according to the chosen scheme.

Again, these modifications are based on the idea that the diffusive contributions should be scaled by the velocity magnitude, rather than by the speed of sound, as the local Mach number decreases. The actual means of ensuring this scaling depends on the choice of preconditioner, through the use of the eigenvalues of the preconditioned system. Other low-diffusion upwinding schemes[1,2,6] can also be extended in a similar manner, and other preconditioners[9,13] could be used.

## V. Results

The modified AUSM+/AUSMDV formulations, extended to generalized coordinates, have been incorporated into an implicit Navier–Stokes solver with multigrid, time-derivative preconditioning and general finite rate chemistry capability.[18] Slope-limited Fromm-type interpolations of the primitive variable vector $[p, u, v, T]^T$ are used to extend the basic first-order formulations to second-order spatial accuracy for some calculations. Further details regarding this extension can be found in Ref. 6. Characteristic boundary conditions based on the eigensystem of the preconditioned equations are employed. The subsections that follow describe the performance of AUSM+(P) and AUSMDV(P) for a selection of test cases.

**Inviscid Flow Past a Bump in a Channel**

Figure 1 shows the behavior of first-order implementations of the schemes for Mach 0.01 inviscid flow over a 10% circular arc bump ($129 \times 65$ mesh). Without preconditioning, the first-order AUSM+ results are completely unphysical (Fig. 1a), as the excess diffusion inherent in the pressure flux splitting corrupts the solution. The solution provided by AUSM+(P) using the Mach number definitions in Eqs. (33) and (34) but without including the pressure–velocity coupling term in Eq. (43) (Fig. 1b) shows marked improvement but reveals a tendency toward odd–even decoupling. This behavior is corrected by AUSM+(P) and AUSMDV(P) (Figs. 1c and 1d). Both produce a nearly symmetric solution, except near the trailing edge of the bump, where first-order slip-surface boundary conditions contaminate the solution slightly. Note that results similar to that shown in Fig. 1b can be obtained through the use of a gauge pressure in the unmodified pressure flux splitting, Eq. (18). This simple expedient

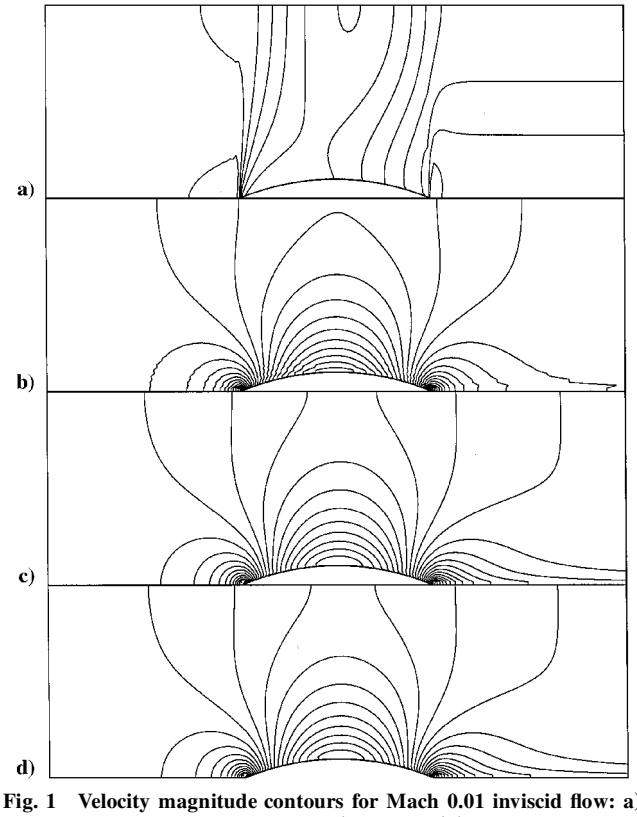


**Fig. 1 Velocity magnitude contours for Mach 0.01 inviscid flow: a) AUSM+ without preconditioning, b) AUSM+(P) without pressure–velocity coupling, c) AUSM+(P), and d) AUSMDV(P).**

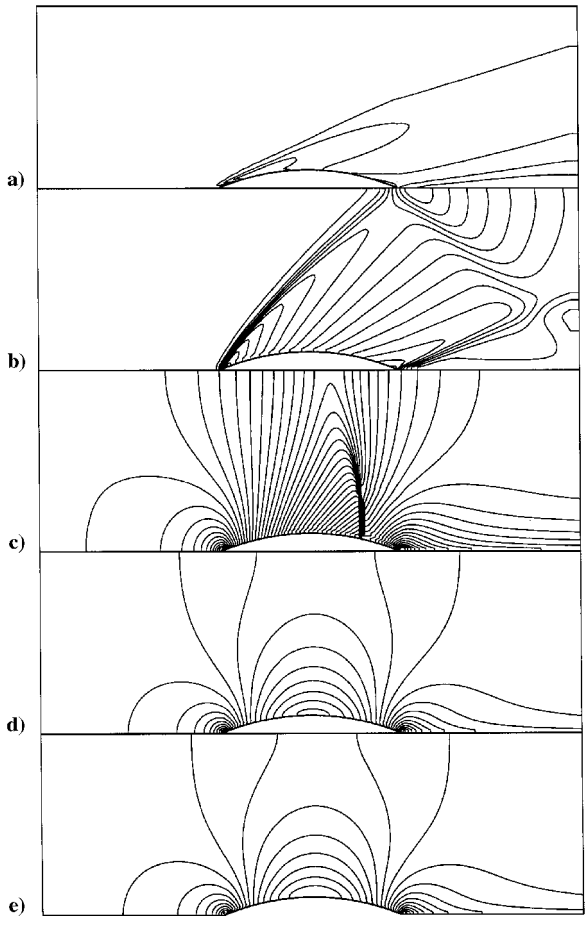


**Fig. 2 Velocity magnitude contours, AUSM+(P): a) $M_\infty = 5$, b) $M_\infty = 2$, c) $M_\infty = 0.675$, d) $M_\infty = 0.2$, and e) $M_\infty = 0.001$.**

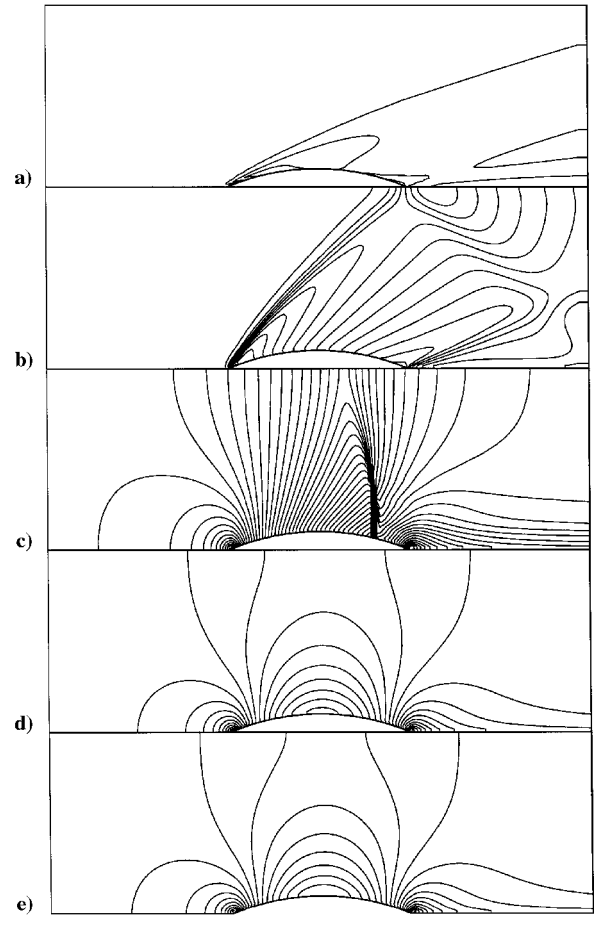


**Fig. 3 Velocity magnitude contours, AUSMDV(P): a) $M_\infty = 5$, b) $M_\infty = 2$, c) $M_\infty = 0.675$, d) $M_\infty = 0.2$, and e) $M_\infty = 0.001$.**

results in odd–even decoupling for higher-speed flows, whereas the use of Eqs. (33) and (34) to scale the pressure flux splitting produces oscillation-free results independent of the flow speed.

Figures 2 and 3 provide an indication of the behavior of first-order implementations of AUSM+(P) and AUSMDV(P) for a range of Mach numbers. The schemes respond similarly for the subsonic cases (Figs. 2d, 2e, 3d, and 3e) but differ for transonic and supersonic conditions (Figs. 2a–2c and 3a–3c) . In particular, it appears that AUSMDV(P) is slightly more diffusive than AUSM+(P) for higher speeds, an effect related to the retention of a pressure-diffusion mechanism at all speeds for AUSMDV(P). Convergence histories for AUSM+(P) are shown in Fig. 4. Flow-independent convergence rates are not quite observed, with the transonic $M_\infty = 0.675$ calculation taking slightly longer than the others and the $M_\infty = 0.001$ calculation leveling out due to round-off errors after a residual reduction of five orders of magnitude. Nevertheless, good efficiency across the Mach number range is obtained.

The influences of preconditioning on the transonic flow predictions ($M_\infty = 0.675$) are highlighted in Fig. 5. The placement and structure of the normal shock wave are captured nearly identically by all methods, but the baseline AUSM+ and AUSMDV schemes do resolve the shock more crisply. This indicates that the influences of preconditioning may need to be terminated slightly before the sonic speed is reached to ensure a higher level of accuracy for transonic flow calculations. One means of accomplishing this has been proposed in Ref. 10 but has yet to be tested in the present work.

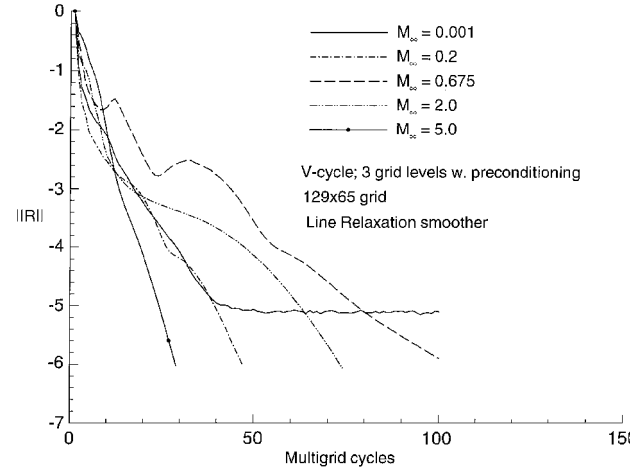


**Fig. 4 Convergence histories: first-order AUSM+(P).**

### Developing Flow in a Channel

A developing viscous flow in a channel is considered as the second test case. This flow has been used extensively in the validation of incompressible flow solvers, and several computational databases are available for comparison (Ref. 19, for example, and others cited therein). In this calculation and those that follow, the freestream pressure and temperature are fixed at 1 atm and 300 K, and the freestream velocity and domain size are adjusted to provide the correct Reynolds number. (This procedure is necessary as the code described in Ref. 18 solves for dimensional variables.) For this particular case, the inflow velocity is chosen as 1 m/s ($M_\infty = 0.0029$), the Reynolds number based on the channel height $D$ is 200, and centerline symmetry is enforced. A $241 \times 65$ grid, clustered slightly to the channel wall, is used for most of the calculations, with grid independence checked for AUSM+(P) through simulations on $121 \times 33$ and $241 \times 129$ meshes. Figures 6 and 7 compare first- and second-order solutions provided by AUSM+(P) and AUSMDV(P) with data from Morihara and Cheng,[20] extracted from Ref. 20 using a digital scanner. The first-order results ($241 \times 65$ grid) differ only slightly from the second-order results, indicating that the low-diffusion properties of AUSM+/AUSMDV in the capturing of viscous layers hold

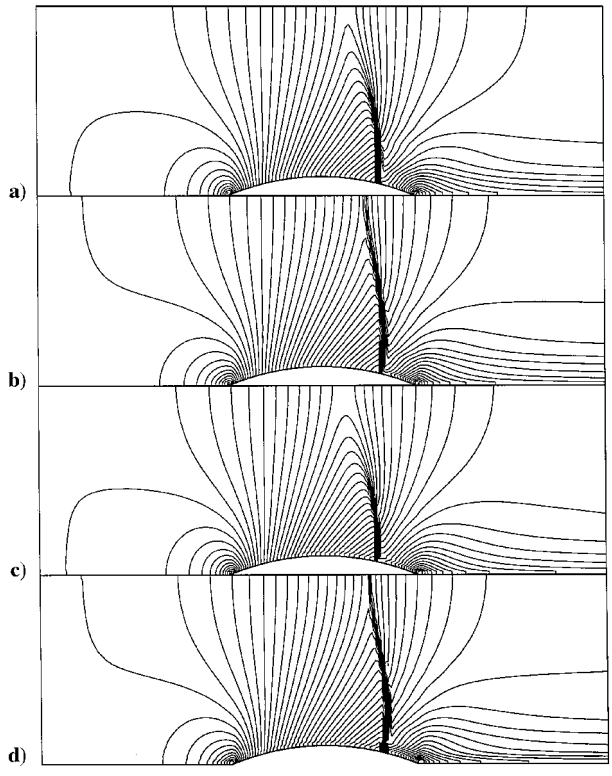


**Fig. 5 Velocity magnitude contours at transonic conditions, first order, $M_\infty = 0.675$: a) AUSM+, b) AUSM+(P), c) AUSMDV, and d) AUSMDV(P).**

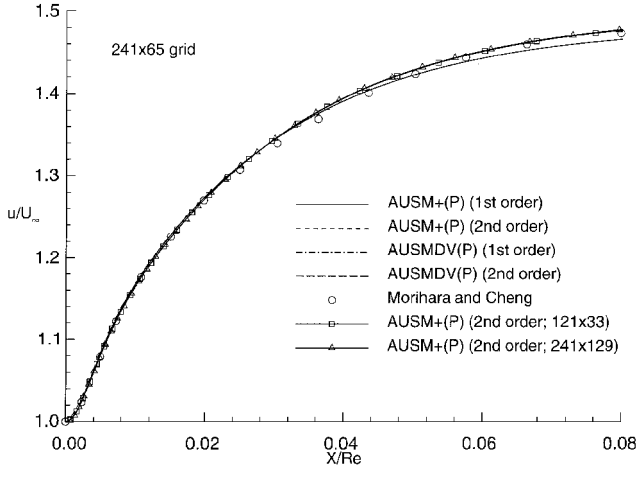


**Fig. 6 Centerline velocity distribution: developing channel flow ($Re = 200$).**

true in the preconditioned extensions. The characteristic inflection point in the velocity profile near the entrance of the channel is clearly captured (Fig. 7), although the peak value is somewhat lower than that predicted by Morihara and Cheng.[20] The earlier simulation was performed on $20 \times 10$ and $40 \times 20$ meshes, compared with the finer meshes used in the current calculation. It is, therefore, possible that the discrepancies evident in the comparison could be a consequence of the mesh resolution. Both first- and second-order AUSM+(P) and AUSMDV(P) solutions collapse upon one another, again indicating that the formulations become nearly equivalent for low-speed flows. The AUSM+(P) predictions also appear to be grid independent. The multigrid convergence rates shown in Fig. 8 are rather insensitive to the mesh size; however, convergence on all grids eventually stalls due to round-off error accumulation. As mentioned earlier, the Navier–Stokes code used in this study solves for dimensional variables and does not utilize gauge pressures or enthalpies. It is probable that the inclusion of these devices, along with a proper nondimensionalization, would improve the convergence behavior.

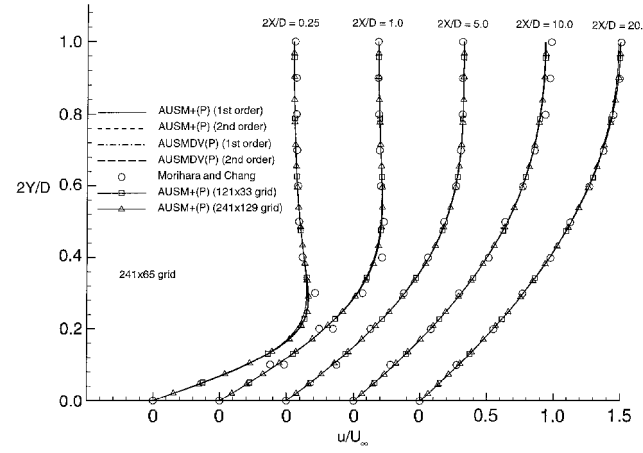


**Fig. 7 Velocity profiles at different $X$ locations: developing channel flow ($Re = 200$).**

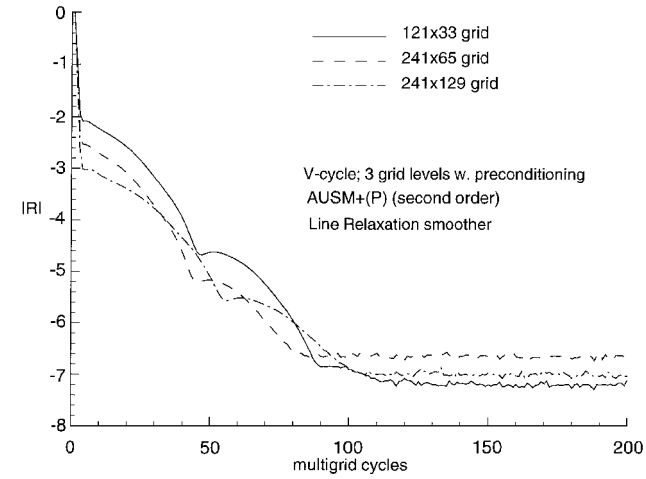


**Fig. 8 Convergence histories for second-order AUSM+(P): developing channel flow ($Re = 200$).**

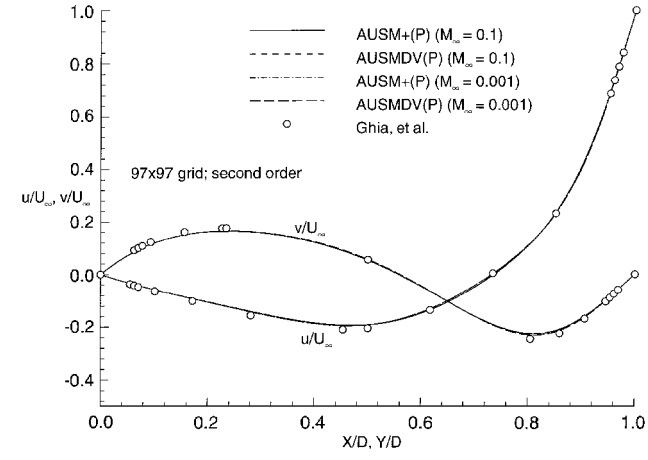


**Fig. 9 Velocity profiles: driven cavity flow ($Re = 100$).**

### Driven-Cavity Flow

The third test case is the well-known driven-cavity problem. Uniformly spaced $97 \times 97$ and $177 \times 177$ grids are utilized, with the cavity dimension again scaled to produce the correct Reynolds number. Figures 9 and 10 compare computed velocity profiles along the $X$ and $Y$ cavity bisectors with the benchmark solutions of Ghia et al.,[21] obtained on a $129 \times 129$ mesh using a stream function-vorticity formulation of the governing equations. Solutions obtained at Mach 0.1 and 0.001 ($Re = 100$) are nearly indistinguishable for both AUSM+(P) and AUSMDV(P) (Fig. 9), and excellent agreement with the benchmark solution is obtained. Results obtained for

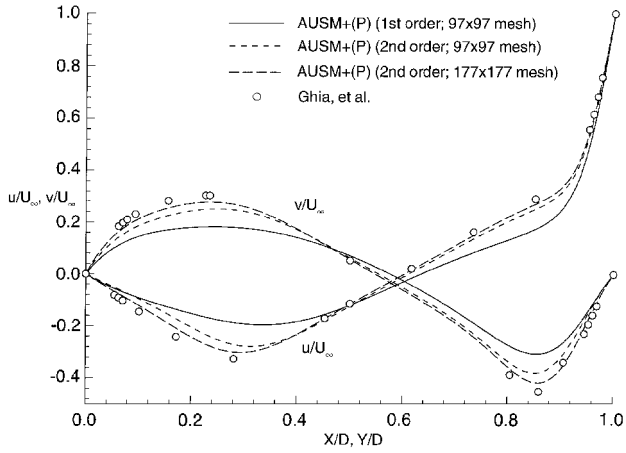


**Fig. 10 Velocity profiles: driven cavity flow ($Re$ = 400).**

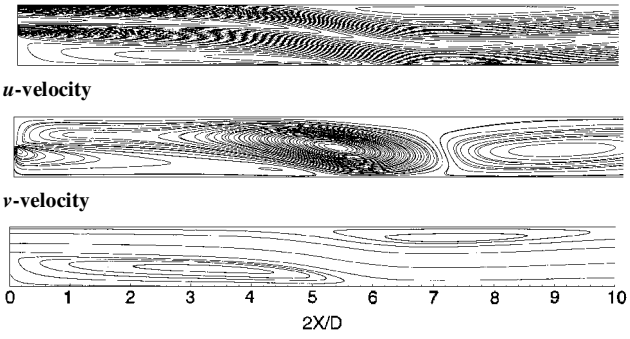


**Fig. 11 Structure of backward-facing-step flowfield ($Re$ = 800); 305 × 65 mesh; second-order AUSM+(P).**

AUSM+(P) at Mach 0.001, $Re = 400$ (Fig. 10), show that first-order accuracy is insufficient for strongly recirculating flows, as the low-diffusion traits of the schemes do not hold for situations in which the velocity components are of the same order. Furthermore, the second-order results are sensitive to the mesh resolution; a 177 × 177 mesh is required to produce reasonable agreement with the benchmark solutions. The reasons for the discrepancies evident in Fig. 10 are unclear. The agreement does improve with some mesh clustering to the walls, however, indicating that differences in wall boundary conditions between primitive-variable and streamfunction-vorticity formulations may play a role.

### Flow Past a Backward-Facing Step

The classical problem of incompressible flow past a backward-facing step in a channel is considered as the fourth test case. The initial pressure and temperature are again 1 atm and 300 K, and a parabolic velocity profile with an average velocity of 1 m/s is specified at the inlet of the channel. The Reynolds number based on the channel height $D$ and the average velocity is 800, and the $X$ extent of the domain is 30 channel heights. A 305 × 65 grid is used, with 241 points uniformly spaced in the streamwise direction from $X/D = 0$ to 15. The remaining 64 nodes expand slowly from $X/D = 15$ to 30. The grid spacing is uniform in the $Y$ direction. These conditions are nearly identical to those employed in Refs. 22 and 23. In Ref. 23, the possibility of attaining unsteady solutions for this case is discussed in detail. In common with most of the tested incompressible flow solvers, the current second-order methods attain a steady solution, albeit somewhat slowly. The dominant features of the backward-facing-step flowfield are the two large recirculation zones, positioned aft of the step and along the top wall of the channel (Fig. 11). Upon reattachment, the flow slowly recovers toward a fully developed Poiseuille flow near the exit of the domain. To predict the structure of the recirculation zones properly, the numerical formulation must capture the response of the pressure field correctly and must not introduce unphysical artificial diffusion. Normalized shear stress plots along the upper and lower surfaces of the channel (Fig. 12) indicate that AUSM+(P) and AUSMDV(P) both meet these criteria. Agreement with the benchmark solution of Gartling[22] is excellent, particularly in the capturing of the separation and reattachment points. Slight discrepancies near the peak values and farther downstream may be a result of inaccuracies in the digital scanning process used to extract the Gartling data. Again, differences between the AUSM+(P) and AUSMDV(P) solutions are minor.

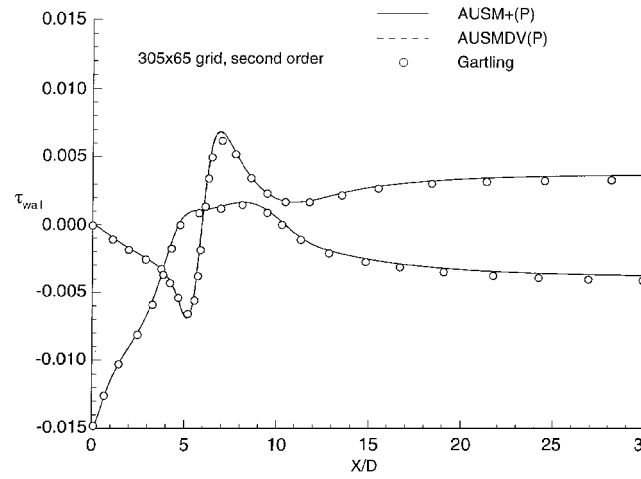


**Fig. 12 Wall shear stress comparisons: backward-facing-step flowfield ($Re$ = 800).**

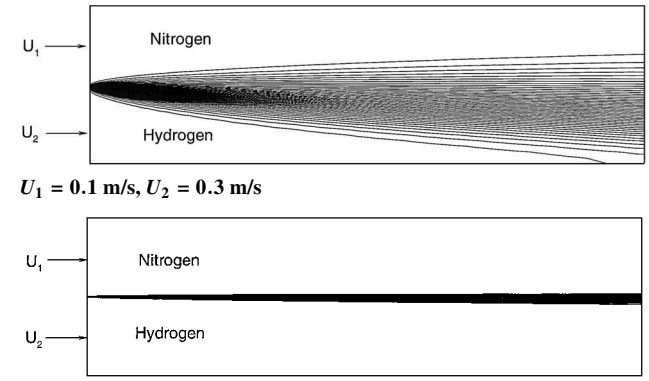


**Fig. 13 Hydrogen mass fraction contours: 65 × 65 mesh; second-order AUSM+(P).**

### Laminar Hydrogen–Nitrogen Mixing Layer

A laminar hydrogen–nitrogen mixing layer is used to test the performance of the discretization methods for low-speed flows with strong density variation due to composition changes. This particular calculation employs a straightforward extension of the low-diffusion flux-splitting concepts to multicomponent gas mixtures.[6] In this extension, the convective transport vector in Eq. (13) is replaced by $[Y_s, u, v, H]^T$, where $Y_s$ is the mass fraction of species $s$ (Ref. 18). The enthalpy, density, and pressure are defined using suitable mixing rules, and the speed of sound in Eq. (15) is replaced by its chemically frozen value. The matrix preconditioner is constructed to solve for the variable vector $[p_s, u, v, T]^T$, where $p_s$ is the partial pressure of species $s$ (Ref. 18). The velocity for the hydrogen stream is chosen as 0.3 and 30 m/s, and the velocity for the nitrogen stream is fixed at three times that of the hydrogen stream. The temperature and pressure are again specified as 300 K and 1 atm. Figure 13 plots the hydrogen mass fraction for the AUSM+(P) simulations, which were performed on a 65 × 65 mesh clustered to the juncture between the fluid streams. The effects of Reynolds number on the growth rate of the mixing layer are clearly indicated. Figures 14 and 15 plot the velocity and density profiles for first- and second-order AUSM+(P) and AUSMDV(P) discretizations. Differences between the first- and second-order predictions are minor, as expected for this free-shear flow. For the lower-speed case (Fig. 14), the AUSM+(P)

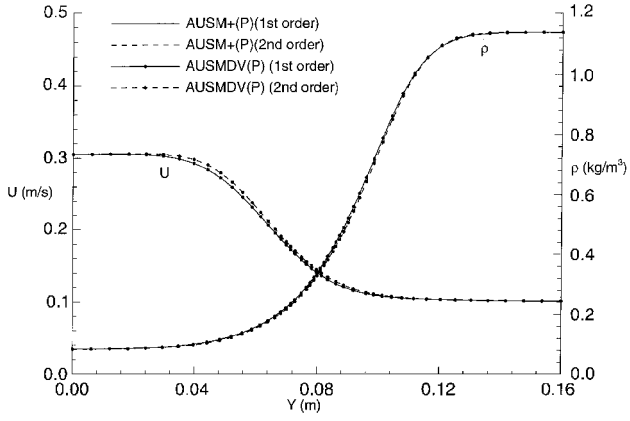


**Fig. 14 Velocity and density profiles: $U_1$ = 0.1 m/s, $U_2$ = 0.3 m/s, and $X$ = 0.7 m.**

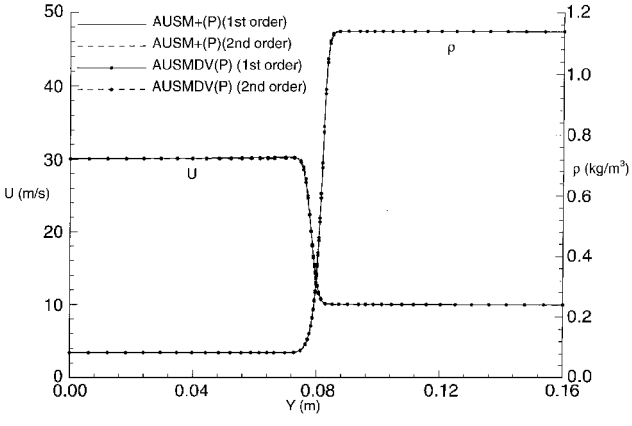


**Fig. 15 Velocity and density profiles: $U_1$ = 10 m/s, $U_2$ = 30 m/s, and $X$ = 0.7 m.**

and AUSMDV(P) results are indistinguishable, indicating that the near equivalence between the schemes for very low Mach numbers also holds in the presence of strong density gradients. For the higher-speed case, minor differences between the AUSM+(P) and AUSMDV(P) predictions begin to emerge (Fig. 15).

## VI Conclusions

A framework for extending low-diffusion flux-splitting schemes to operate effectively in conjunction with time-derivative preconditioning has been presented. Results for two representative methods, AUSM+ and AUSMDV, indicate that the modifications proposed are effective in maintaining solution accuracy and efficiency for flow calculations at all speeds. When extended to second-order accuracy, the new schemes provide solutions in agreement with classical benchmark studies for incompressible, recirculating flows, whereas for nominally parabolic flows, even first-order results are acceptable. The schemes also perform well for very low-speed flows with significant density variation and transition smoothly to the original formulations as the local Mach number approaches unity. Although not indicated in the present validative study, the schemes have been successfully used for reacting flow calculations at all speeds as well as unsteady flow simulations.

## Acknowledgments

Part of this work was accomplished while the first author was in residence at the Institute for Computational Mechanics in Propulsion at NASA Lewis Research Center. Cray Y-MP and Cray T-90 computing time was provided by grants from NASA Lewis Research Center and the North Carolina Supercomputing Center. Thanks are extended to Peter Sockol, NASA Lewis Research Center, for his suggestions of appropriate low-speed test cases.

## References

[1]Liou, M.-S., and Steffen, C. J., "A New Flux Splitting Scheme," NASA TM-104404, May, 1991; also *Journal of Computational Physics*, Vol. 107, No. 1, 1993, pp. 23–39.

[2]Coquel, F., and Liou, M.-S., "Field by Field Hybrid Upwind Splitting Methods," *Proceedings of the AIAA 11th Computational Fluid Dynamics Conference*, AIAA, Washington, DC, 1993, pp. 51–61 (AIAA Paper 93-3302).

[3]Wada, Y., and Liou, M.-S., "A Flux Splitting Scheme with High-Resolution and Robustness for Discontinuities," AIAA Paper 94-0083, Jan. 1994.

[4]Liou, M.-S., "A Continuing Search for a Near-Perfect Numerical Flux Scheme—Part 1: AUSM+," NASA TM-106524, March 1994.

[5]Liou, M.-S., "Progress Towards an Improved CFD Method: AUSM+," *Proceedings of the AIAA 12th Computational Fluid Dynamics Conference*, AIAA, Washington, DC, 1995, pp. 606–625 (AIAA Paper 95-1701).

[6]Edwards, J. R., "A Low-Diffusion Flux-Splitting Scheme for Navier–Stokes Calculations," *Computers and Fluids*, Vol. 26, No. 6, 1997, pp. 635–659.

[7]Liou, M.-S., "Probing Numerical Fluxes: Mass Flux, Positivity, and Entropy-Satisfying Property," *Proceedings of the AIAA 13th Computational Fluid Dynamics Conference*, AIAA, Reston, VA, 1997, pp. 943–954 (AIAA Paper 97-2035).

[8]Choi, Y. H., and Merkle, C. L., "The Application of Preconditioning in Viscous Flows," *Journal of Computational Physics*, Vol. 105, No. 2, 1993, pp. 207–223.

[9]Van Leer, B., Lee, W. T., and Roe, P. L., "Characteristic Time Stepping or Local Preconditioning of the Euler Equations," AIAA Paper 91-1552, July 1991.

[10]Turkel, E., Vatsa, V. N., and Radespiel, R., "Preconditioning Methods for Low-Speed Flows," AIAA Paper 96-2460, June 1996.

[11]Weiss, J. M., and Smith, W. A., "Preconditioning Applied to Variable and Constant Density Time-Accurate Flows on Unstructured Meshes," AIAA Paper 94-2209, June 1994.

[12]Merkle, C. L., Venkateswaran, S., and Buelow, P. E. O., "The Relationship Between Pressure-Based and Density-Based Algorithms," AIAA Paper 92-0425, Jan. 1992.

[13]Dailey, L. D., and Pletcher, R. H., "Evaluation of Multigrid Acceleration for Preconditioned, Time-Accurate Navier–Stokes Algorithms," AIAA Paper 95-1668, June 1995.

[14]Wang, Z. J., "A Fast Flux-Splitting for All Speed Flow," *Proceedings of 15th International Conference on Numerical Methods in Fluid Dynamics*, June 1996.

[15]Jameson, A., "Artificial Diffusion, Upwind Biasing, Limiters, and Their Effect on Accuracy and Multigrid Convergence in Transonic and Hypersonic Flow," AIAA Paper 93-3559, July 1993.

[16]Tweedt, D. L., Chima, R. V., and Turkel, E., "Preconditioning for Numerical Simulation of Low Mach Number Three-Dimensional Viscous Turbomachinery Flows," AIAA Paper 97-1828, June 1997.

[17]Rhie, C. M., and Chow, W. L., "A Numerical Study of the Turbulent Flow Past an Isolated Airfoil with Trailing Edge Separation," AIAA Paper 82-0998, Jan. 1982.

[18]Edwards, J. R., and Roy, C. J., "Preconditioned Multigrid Methods for Two-Dimensional Combustion Calculations at All Speeds," *AIAA Journal*, Vol. 36, No. 2, 1998, pp. 185–192.

[19]Chen, K.-H., and Pletcher, R. H., "Primitive Variable, Strongly Implicit Calculation Procedure for Viscous Flows at All Speeds," *AIAA Journal*, Vol. 29, No. 8, 1991, pp. 1241–1249.

[20]Morihara, H., and Cheng, R. T., "Numerical Solution of the Viscous Flow in Entrance Region of Parallel Plates," *Journal of Computational Physics*, Vol. 11, No. 4, 1973, pp. 550–572.

[21]Ghia, U., Ghia, K. N., and Shin, C. T., "High-Re Solutions for Incompressible Flow Using the Navier–Stokes Equations and a Multigrid Method," *Journal of Computational Physics*, Vol. 48, No. 3, 1982, pp. 387–411.

[22]Gartling, D., "A Test Problem for Outflow Boundary Conditions—Flow over a Backward-Facing Step," *International Journal for Numerical Methods in Fluids*, Vol. 11, No. 7, 1990, pp. 953–967.

[23]Gresho, P., Gartling, D., Torczynski, J. R., Cliffe, K. A., Winters, K. H., Garratt, T. J., Spence, A., and Goodrich, J. W., "Is the Steady Viscous Incompressible Two-Dimensional Flow over a Backward Facing Step at $Re = 800$ Stable?" *International Journal for Numerical Methods in Fluids*, Vol. 17, No. 6, 1993, pp. 501–541.

J. Kallinderis
*Associate Editor*